Interface-Engineered $(AlMnCoNiZn)_3O_4$@PPy nanocomposites for Superior Lithium Storage: Mechanism and Performance

Yunhe Liang[1], Changqing Jin[1]*, Dengyu Tian[1], Zaidong Peng[1], Zhong Yang[1], Qingping Ding[2]*

[1] Shaanxi Key Laboratory of Optoelectronic Functional Materials and Devices, School of Materials and Chemical Engineering, Xi'an Technological University, Xi'an 710021, People's Republic of China

[2]Ames National Laboratory, U.S. DOE, and Department of Physics and Astronomy, Iowa State University, Ames, Iowa 50011, USA

*** Correspondence:**
Corresponding Author
eaglejin@xatu.edu.cn; qpding@ameslab.gov

Abstract: The practical application of graphite anodes in lithium-ion batteries (LIBs) is constrained by low specific capacity (372 mAh g-1) and sluggish kinetics. To address these limitations, our present study focuses on high-entropy oxides (HEOs), which offer high theoretical capacity and structural stability. We synthesized spinel-structured $(AlMnCoNiZn)_3O_4$ nanoparticles via a solution combustion method and fabricated an $(AlMnCoNiZn)_3O_4$@polypyrrole (PPy) nanocomposite through in-situ polymerization. Our electrochemical tests demonstrate that the PPy modification significantly enhances performance. While the pristine $(AlMnCoNiZn)_3O_4$ delivered 445 mAh g^{-1} after 100 cycles at 100 mA g^{-1} and 350 mAh g^{-1} after 1000 cycles at 1000 mA g^{-1}, the $(AlMnCoNiZn)_3O_4$@PPy composite achieved 695 mAh g^{-1} after 100 cycles and maintained 675 mAh g^{-1} after 1000 cycles. Furthermore, the composite improved rate capacity at 1000 mA g^{-1} from 211 mAh g^{-1} to 403 mAh g^{-1}. This work highlights how conductive and flexible polymer modifications can dramatically improve the electrochemical properties of HEOs. The developed $(AlMnCoNiZn)_3O_4$@PPy composite provides a promising direction for designing advanced anodes to meet next-generation energy storage demands.

Key words: Lithium-ion battery; Anodes material; High entropy oxide; Nanocomposites; Electrochemical performance

1. Introduction

Lithium-ion batteries (LIBs) are widely used in portable electronics, electric vehicles, and grid-scale storage due to their high energy density and long cycle life. However, increasing demands for safety and stability require further enhancements [1,2]. While commercial graphite anodes are cost-effective, their low theoretical capacity (372 mAh g^{-1}) and tendency to form lithium dendrites at high rates limit their use in next-generation high-energy batteries [3-5].

Alloy-type materials (e.g., Si, Sn) offer higher capacities but suffer from severe volume expansion (300-400%), leading to rapid capacity fading [6,7]. Conversely, $Li_4Ti_5O_{12}$ offers "zero-strain" stability but is hindered by low capacity (175 mAh g^{-1}) and gas evolution [8,9]. Thus, developing anode materials that combine high capacity, structural robustness, and rapid kinetics is essential [10].

High-entropy oxides (HEOs) have emerged as promising candidates due to their multi-cationic compositions, tunable redox activity, and enhanced diffusion kinetics. Following the initial report of entropy-stabilized oxides by Rost et al. in 2015 [11], Sarkar et al. demonstrated their potential as LIB electrodes in 2018 [12]. Nevertheless, HEOs face challenges typical of conversion-type anodes, including significant volume changes and low electronic conductivity [13-15].

Interface engineering with conductive matrices like Polypyrrole (PPy) can mitigate these issues [16,17]. Our previous work on $(CrMnCoNiZn)_3O_4$@PPy utilized PPy's conductivity and buffering effects [18-20]. However, the high-valence chromium (Cr^{3+}/Cr^{6+}) involved in reduction reactions introduced structural instability and volume strain. In this study, we investigate the $(AlMnCoNiZn)_3O_4$@PPy composite, replacing the electrochemically active Cr with inert Al to improve stability.

Our work addresses three critical challenges: (i) suppressing parasitic side reactions to enhance initial coulombic efficiency (ICE); (ii) improving electronic/ionic conductivity; and (iii) utilizing the mechanical flexibility of PPy to accommodate volumetric strain.

We synthesized spinel-type $(AlMnCoNiZn)_3O_4$ nanoparticles via solution combustion and constructed core-shell $(AlMnCoNiZn)_3O_4$@PPy nanocomposites through in situ polymerization. The resulting material achieved a reversible capacity of 675 mAh g^{-1} after 1000 cycles at 1 1000 mA g^{-1}, a 60% improvement over the Cr-based equivalent (416 mAh g^{-1}). This study demonstrates that substituting active Cr with inert Al, combined with PPy interface modification, provides a scalable strategy for high-performance HEO-based anodes.

2. Experimental section

2.1 Synthesis of $(AlMnCoNiZn)_3O_4$ via Solution Combustion Method

The HEO $(AlMnCoNiZn)_3O_4$, was synthesized using a solution combustion approach as described in our previous work [20-22]. Stoichiometric amounts of metal nitrates—$Al(NO_3)_3 \cdot 9H_2O$ (0.9378 g), $Mn(NO_3)_2 \cdot 4H_2O$ (0.8948 g), $Co(NO_3)_2 \cdot 6H_2O$

(0.7276 g), $Ni(NO_3)_2 \cdot 6H_2O$ (0.7270 g), and Zn(NO3)2·6H2O (0.7437 g)—were dissolved in deionized water under vigorous stirring. Subsequently, 0.4692 g of glycine ($C_2H_5NO_2$) was added as a combustion fuel to the homogeneous solution, which was then dried to form a viscous gel. The gel was subjected to combustion in a muffle furnace at 750 °C under ambient air for 40 minutes. After natural cooling, the resulting $(AlMnCoNiZn)_3O_4$ product was obtained and designated as HEO.

2.2 Preparation of $(AlMnCoNiZn)_3O_4$@PPy nanocomposite via in-situ polymerization

The $(AlMnCoNiZn)_3O_4$@PPy composite (designated as HEO@PPy) was fabricated through in-situ oxidative polymerization according to the following procedure:

1. Dispersion: 0.1 g of HEO powder was dispersed in 100 mL of deionized water via ultrasonication (40 kHz, 30 min).

2. Surfactant Addition: Cetyltrimethylammonium bromide (CTAB, molar ratio CTAB:Py = 1:3) was added as a surfactant, followed by magnetic stirring (500 rpm, 15 min) to achieve a homogeneous dispersion.

3. Monomer and Oxidant Injection: Under continuous stirring, 0.2 mL of pyrrole monomer (Py) was injected dropwise into the suspension, immediately followed by the addition of $FeCl_3$ oxidant (molar ratio $FeCl_3$:Py = 2:1).

4. Polymerization: The reaction was conducted in an ice bath (0-4°C) for 6 h with constant stirring (300 rpm).

5. Recovery and Drying: The resulting black precipitate was collected by centrifugation (8000 rpm, 10 min), washed three times each with ethanol and deionized water, and vacuum-dried at 60°C for 12 h before being ground into a final powder.

2.3. Structural and chemical characterization

The crystalline phases of the synthesized materials were analyzed via X-ray diffraction (XRD) using a Bruker D2 with Cu Kα radiation (λ = 1.5406 Å) at a scanning rate of 2° min^{-1} over a 2θ range of 10–80°. Morphological evaluation and high-resolution lattice imaging were performed using transmission electron microscopy (TEM, JEM-2010) operated at 200 kV. Samples were prepared by dispersing powders in ethanol and depositing them onto carbon-coated copper grids. Energy-dispersive spectroscopy (EDS) integrated into the TEM was employed to investigate elemental distribution. The molecular structure of the samples was characterized by Raman spectroscopy using a LabRAM HR Evolution spectrometer (Horiba Scientific, France) with a 532 nm excitation laser at 5 mW power. Additionally, the valence states and elemental composition were determined by X-ray photoelectron spectroscopy (XPS) using a Thermo Scientific K-Alpha system. All acquired data were calibrated against the C 1s peak at 284.8 eV.

2.3. Electrode fabrication and electrochemical characterization

The working electrode was prepared by mixing the active material, Super P conductive carbon, and polyvinylidene fluoride (PVDF) binder at a mass ratio of 7:2:1. The PVDF was first dissolved in N-methyl-2-pyrrolidone (NMP) under continuous stirring for 6–8 h. The resulting mixture was uniformly coated onto a copper foil current collector using a doctor blade and vacuum-dried at 80°C for 12 h. The dried electrode was cut into 12 mm diameter discs and compacted under mechanical pressure to enhance interfacial contact. Finally, the electrodes were baked at 120°C under vacuum for an additional 12 h before assembly. Each electrode was loaded with approximately 1 mg of active material, yielding an areal loading of ~0.7 mg cm^{-2}. During CR2032 coin cell assembly, 50 μL of electrolyte was introduced, with 30 μL dispensed on the active material side and 20 μL on the lithium metal side of the separator. Electrochemical performance was evaluated using a Neware Electronics CT-4008 battery test system.

Cells were subjected to galvanostatic charge-discharge testing and galvanostatic intermittent titration technique (GITT) measurements within a potential window of 0.01–3.0 V (vs. Li^+/Li). To evaluate rate capability and long-term cycling stability, current densities of 0.1, 0.2, 0.5, 1, 2, and 0.1 A g-1 were applied. The rate-dependent electrochemical response was systematically analyzed to determine kinetic limitations.

Cyclic voltammetry (CV) was performed using a CHI660E electrochemical workstation at a scan rate of 0.1 mV s^{-1} (0.01–3.0 V) to identify redox reactions and reversibility. Finally, electrochemical impedance spectroscopy (EIS) measurements were conducted from 10^6 to 10^{-2} Hz with an AC amplitude of 5 mV to evaluate charge-transfer resistance and interfacial kinetics.

3. Result and discussion

Figure 1a presents the X-ray diffraction (XRD) pattern of the synthesized $(AlMnCoNiZn)_3O_4$ HEO nanoparticles. The sharp and symmetric diffraction peaks correspond exclusively to the characteristic reflections of a spinel structure. The absence of detectable impurity phases confirms the successful formation of a phase-pure spinel-type HEO. Furthermore, Rietveld refinement demonstrated excellent agreement between experimental data and theoretical simulation, yielding a calculated material density of 8.91 g/cm^3 and a goodness-of-fit (χ^2) of 2.09. The agreement factors (Rwp = 1.71%, Rp = 1.31%) are both significantly below the 7% threshold. In comparison, Figure 1b displays the XRD pattern of the $(AlMnCoNiZn)_3O_4$@PPy composite. While the composite maintains all fundamental spinel-phase features, it also incorporates a broad amorphous hump centered at $2\theta \approx 20°$, which is characteristic of the non-crystalline structure of polypyrrole [20, 23, 24]. These results confirm that the conductive polymer coating process preserves the crystalline integrity of the host oxide without inducing phase transformations or secondary phase formation.

Raman spectroscopic analysis, shown in Figure 1c, confirms the successful incorporation of PPy within the HEO matrix. The composite's Raman spectrum demonstrates distinct vibrational signatures from both constituent phases: (1)

Characteristic PPy modes at 1566 cm^{-1} (C=C backbone stretching), 1367 cm^{-1} (pyrrole ring stretching), and 1055 cm^{-1} (C-H in-plane deformation) [20, 25]; (2) Prominent HEO phonon modes at 525 cm^{-1} (F_{2g}) and 616 cm^{-1} (A_{1g}).The F_{2g} Raman band is attributed to the asymmetric stretching vibration of metal-oxygen bonds at tetrahedral sites, providing direct evidence of cationic disorder induced by configurational entropy in the synthesized HEO nanoparticles [26]. Meanwhile, the A1g mode corresponds to the symmetric vibration along the oxygen-to-tetrahedral-cation bond axis [27].

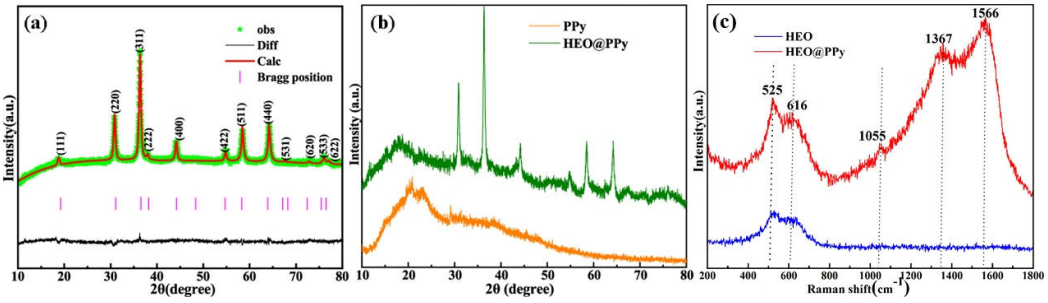

Fig. 1. XRD patterns of the (a) HEO nanoparticles; (b) HEO@PPy nanocomposite. (c) Raman spectra of the samples.

To further investigate the microstructural surface characteristics of the $(AlMnCoNiZn)_3O_4$@PPy composite, TEM and high-resolution TEM (HRTEM) were employed, as depicted in Fig. 2. Fig. 2a demonstrates that the nanocomposite exhibits a relatively uniform particle size distribution, with an average diameter of approximately 60 nm. Fig. 2b clearly displays the well-defined core-shell architecture of the nanocomposite. The TEM image reveals that PPy underwent heterogeneous nucleation on the HEO substrate (denoted as PPyB), while some PPy particles formed aggregates independent of the HEO surface (labeled PPyA). Fig. 2c presents the HRTEM image of HEO@PPy, where lattice fringe spacings of 2.97 Å are observed, corresponding to the (220) crystallographic planes of the spinel-structured HEO phase. Notably, a sharp interface between the crystalline HEO and amorphous PPy is evident, further corroborating the successful fabrication of the HEO@PPy core-shell nanocomposite. During synthesis, the HEO nanoparticles functioned as nucleation sites, facilitating the heterogeneous polymerization and growth of PPy on their surfaces. These results confirm that the crystalline framework of the HEO remains unmodified upon PPy functionalization, maintaining a single-phase spinel configuration.

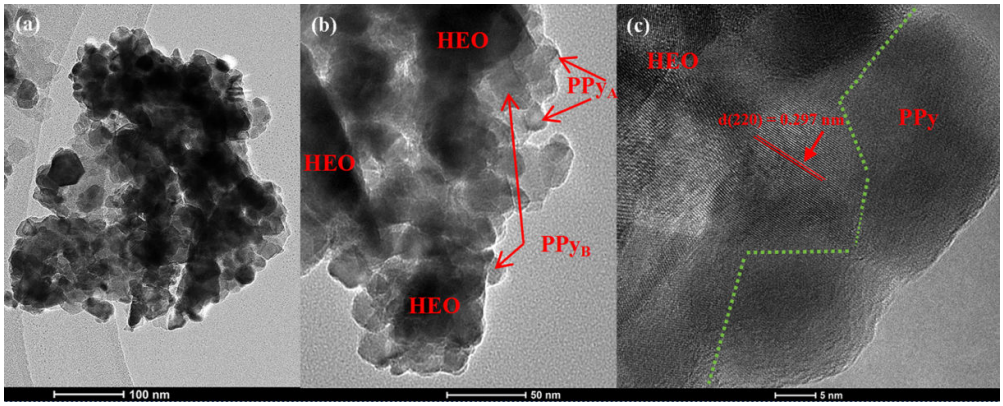

Fig. 2. TEM images of the HEO@PPy at different magnifications (a and b); HRTEM image of the HEO@PPy (c).

To verify the elemental homogeneity of the composite, TEM-EDS mapping was conducted. Figures 3(a–j) display the TEM image and corresponding EDS elemental maps of the HEO@PPy composite, demonstrating a uniform distribution of Al, Mn, Co, Zn, Ni, and O with atomic percentages of 9.04%, 8.73%, 8.82%, 8.64%, 8.98%, and 55.87%, respectively. Notably, all metallic elements exhibit nearly equimolar ratios, aligning with the stoichiometric proportions of the raw materials. Furthermore, the molar ratio of total metallic elements to oxygen is 0.795, closely matching the theoretical value of 0.75 for the spinel structure (AB_2O_4). These results confirm the successful synthesis of spinel-structured HEO. Figures 3i and 3j reveal that the spatial distributions of C and N extend beyond the regions occupied by HEO elements. The carbon distribution exhibits a significantly broader dispersion, likely due to the carbon support film. Nitrogen demonstrates a spatial distribution nearly identical to the metallic and oxygen elements of the HEO phase, showing excellent uniformity. However, trace amounts of nitrogen are detectable at the periphery of the metallic/oxygen distributions. This suggests preferential PPy polymerization on HEO particle surfaces, though minimal PPy formation on container walls or through homogeneous nucleation cannot be entirely excluded. Given this preferential growth, the formation of HEO@PPy composite structures with partial or complete core-shell configurations is thermodynamically favorable. These EDS-mapping conclusions are consistent with the HRTEM characterization, providing definitive evidence for the successful fabrication of core-shell structured HEO@PPy nanocomposites. Additionally, BET measurements were performed on both HEO and HEO@PPy. The observed reduction in specific surface area and pore volume for HEO@PPy indicates successful PPy coating, which likely filled the original pores of the HEO. Detailed BET data are provided in Figure S1 and Table S1 of the Supporting Information.

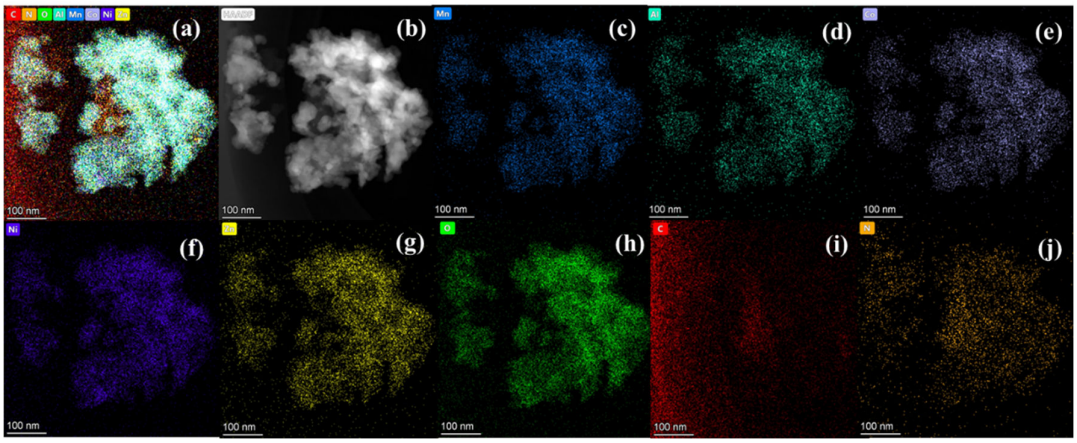

Fig. 3. All elementals EDS-mapping (a), corresponding TEM image (b), and corresponding elemental mapping of Mn (c), Al (d), Co (e), Ni (f), Zn (g), O (h), C (i) and N (j) of the HEO@PPy.

To investigate the electrochemical kinetics and lithium storage mechanism of the samples, cyclic voltammetry (CV) measurements were conducted using lithium metal as the counter electrode and the samples as the working electrode. The CV profile of the HEO presented in Fig. 4a demonstrates distinct electrochemical characteristics. During the initial cathodic scan, a prominent reduction peak emerges within the potential range of 1.1–1.5 V, which is attributed to the reduction of metal oxides to their corresponding metallic states ($M^{n+} \rightarrow M^0$) [28]. Among these elements, Mn, Co, Ni, and Zn serve as electrochemically active components whose rich valence variations contribute to the capacity of the HEO. In contrast, Al exists solely as Al^{3+} and functions to enhance the structural strength of the HEO. Subsequently, a pronounced irreversible reduction peak is observed between 0.1–0.8 V that disappears in subsequent cycles. This phenomenon indicates the formation of a solid electrolyte interphase (SEI) film on the HEO anode surface, accompanied by the generation of Li_2O [29]. In the subsequent anodic scans, the anodic peaks broaden within the 1.5–2.3 V potential window. These peaks correspond to the delithiation process, wherein Li_2O reacts with metallic components to reform metal oxides while releasing lithium ions. Notably, the broad nature of these anodic peaks suggests that the oxidation process likely occurs through a continuous, multi-step mechanism [30]. This observation implies complex reaction kinetics during the delithiation process in the HEO system. The oxidation/reduction reaction at the anode during lithiation/delithiation can be expressed by Eq. (1):

$$\frac{1}{y}M_xO_y + 2Li \Leftrightarrow^{2e} Li_2O + \frac{x}{y}M, M = Mn, Co, Ni, Zn \quad (1)$$

Figure 4b illustrates the CV profiles of the HEO@PPy composite anode during the initial three cycles. The curves exhibit reduction peaks between 1.0–1.5 V and 0.1–0.8 V, alongside corresponding anodic peaks. The HEO@PPy composite maintains similar peak positions and shapes to the pristine HEO anode, suggesting that the PPy coating does not alter the fundamental electrochemical kinetics or lithium storage mechanisms. Notably, fitting calculations show that the irreversible capacity of the pristine HEO anode is 1.83 times higher than that of the HEO@PPy composite, demonstrating that

PPy effectively suppresses irreversible capacity loss.

Figures 4c and 4d present the galvanostatic discharge/charge profiles at a current density of 50 mA g^{-1}. The pristine HEO anode delivers initial capacities of 1974/1063 mAh g^{-1}, while the HEO@PPy composite exhibits 1241/927 mAh g^{-1}. While the PPy coating may slightly reduce initial capacity by limiting direct electrolyte contact at active sites, it significantly mitigates lithium-consuming side reactions. Consequently, the initial coulombic efficiency (ICE) of the HEO@PPy composite reaches 74.6%, markedly higher than the 53.9% of pristine HEO and the 61.7% reported for $(CrMnCoNiZn)_3O_4$@PPy. These results confirm that the PPy layer acts as an effective physical barrier that reduces irreversible capacity and enhances electrochemical reversibility, highlighting the advantages of the Al-based HEO@PPy system.

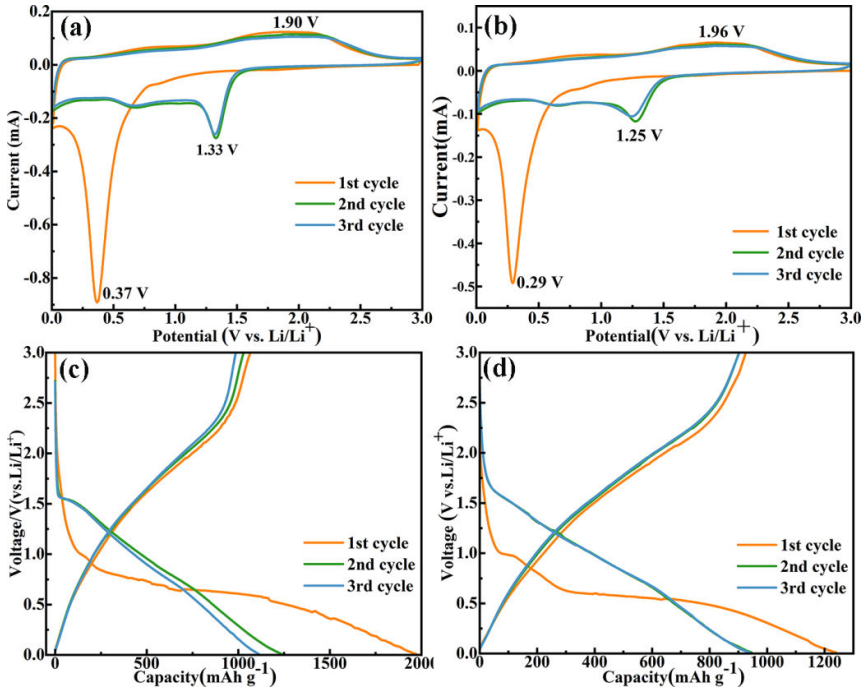

Fig. 4. CV curves at a scan rate of 0.1 mV/s of HEO (a) and HEO@PPy (b); Charge/discharge curves of HEO (c) and HEO@PPy (d).

Fig. 5a compares the cycling performance of HEO and HEO@PPy composite anodes at a current density of 100 mA g^{-1}. The capacity of HEO degrades rapidly during the initial 20 cycles, stabilizes after 60 cycles, and ultimately retains only 445 mAh g^{-1} after 100 cycles. In contrast, the HEO@PPy composite demonstrates a more gradual fade during the first 20 cycles, stabilizes after 70 cycles, and maintains a stable capacity of 695 mAh g^{-1} after 100 cycles. Overall, the HEO@PPy composite exhibits significantly improved cycling stability at this current density.

Fig. 5b presents the long-term cycling performance at 1000 mA g^{-1}. The HEO@PPy composite retains a capacity of 675 mAh g^{-1} after 1,000 cycles, far exceeding the 350 mAh g^{-1} of bare HEO. During charge/discharge, the PPy matrix effectively accommodates the volume strain of the HEO, restricting it within the elastic range to prevent fracture and pulverization. While both electrodes show capacity fading

during the first 100 cycles, the composite degrades more slowly than pristine HEO. Notably, the composite exhibits a distinct capacity recovery: after dropping to 286 mAh g^{-1} at 120 cycles, the capacity gradually increases to 637 mAh g^{-1} by cycle 400. This recovery aligns with reported polymer/gel-film formation and dynamic interfacial reorganization, which activates additional storage sites [31-33]. The sustained performance further reflects how PPy-derived heterointerfaces enable hybrid Li^+ storage.

Fig. 5c evaluates the rate capabilities of both electrodes. The HEO@PPy composite delivers superior performance with capacities of 884, 778, 627, 514, and 403 mAh g^{-1} at 100, 200, 500, 1000, and 2000 mA g^{-1}, respectively. When the current density is restored to 100 mA g^{-1}, the composite maintains 85.3% capacity retention (754 mAh g^{-1}), significantly higher than the 70.5% retention (489 mAh g^{-1}) of bare HEO. This improvement is attributed to the enhanced ionic/electronic conductivity and structural stability provided by the PPy matrix.

Fig. 5d displays the electrochemical impedance spectra (EIS) collected after 10 cycles at 100 mA g^{-1}. The smaller semicircle diameter for HEO@PPy in the mid-frequency region indicates a reduced charge transfer resistance (Rct), while the steeper low-frequency slope suggests improved Li^+ diffusion kinetics. Quantitatively, the Rct of pristine HEO is 535 Ω, whereas that of the HEO@PPy composite is significantly reduced to 278 Ω. Additionally, the lower Warburg impedance (W1) for HEO@PPy suggests faster Li^+ diffusion compared to the unmodified HEO. The Li^+ diffusion coefficient (DLi^+) was calculated using the following equations:

$$D_{Li^+} = \frac{R^2T^2}{2A^2n^4F^4C^4{\sigma_w}^2} \quad (2)$$

$$Z' = R_s + R_{ct} + \sigma_w\sigma^{-1/2} \quad (3)$$

where: R is the universal gas constant, T is the absolute temperature, A is the electrode surface area, n is the number of electrons transferred per redox reaction, F is Faraday's constant, C is the Li^+ concentration, σ_w is the Warburg coefficient (obtained from the slope of the linear region in the low-frequency Warburg impedance plot).

A smaller Warburg slope corresponds to a higher lithium-ion diffusion coefficient D_{Li+}. The calculated D_{Li+} values for HEO and HEO@PPy are 8.89×10^{-16} and 5.3×10^{-15} cm^2s^{-1}, respectively. The lower Rct and higher D_{Li+} of the HEO@PPy composite demonstrate improved electronic and ionic conductivity. In this composite, PPy forms a continuous, highly conductive coating on the HEO surface, connecting individual particles to create a conductive network. This structure optimizes interfacial charge transfer kinetics, improves contact between particles and the electrolyte, and significantly reduces electrode impedance. Consequently, this promotes lithium-ion migration and alleviates kinetic limitations at high rates, synergistically enhancing overall electrochemical performance. These findings align with the observed kinetic advantages in electrochemical lithium storage.

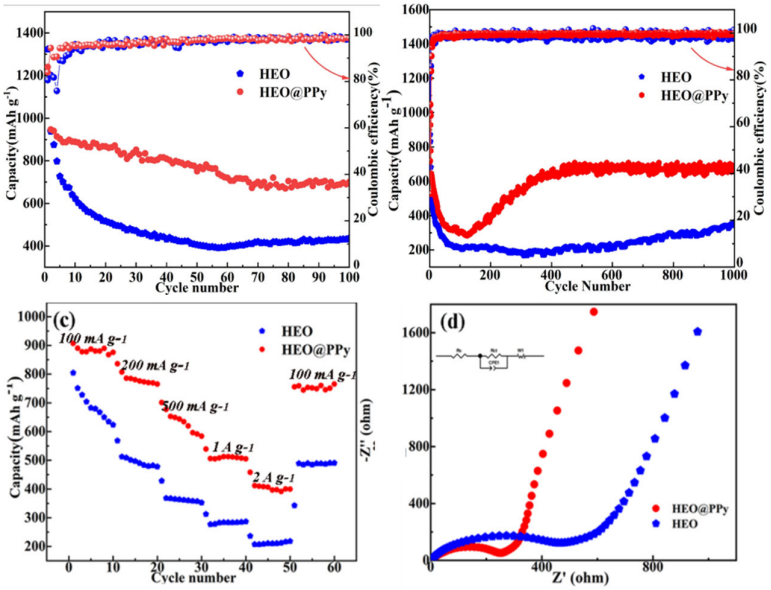

Fig. 5. Electrochemical performance of HEO and HEO@PPy: cycling performance at 100 mA g^{-1} (a); long-term cycling performance at 1 A g^{-1} (b); rate capability (c); EIS spectra (d).

Electrochemical Impedance Spectroscopy (EIS) probes apparent lithium-ion diffusion behavior by analyzing low-frequency Warburg impedance under quasi-equilibrium conditions. However, the measured impedance represents a global response influenced by high interfacial impedance in nanomaterials, interparticle contact resistance, and macroscopic electrode structure. Consequently, EIS often fails to isolate intrinsic lattice diffusion, typically yielding an apparent diffusion coefficient significantly lower than the intrinsic value. This makes EIS better suited for assessing the overall transport performance of practical electrodes rather than determining precise bulk diffusion coefficients. In contrast, the Galvanostatic Intermittent Titration Technique (GITT) is preferred for accurately determining intrinsic diffusion coefficients. GITT operates under non-equilibrium conditions through galvanostatic pulses and relaxation periods, calculating the Li^+ diffusion coefficient based on voltage responses induced by concentration polarization. This method, grounded in Fick's laws, effectively reflects long-range diffusion within the bulk material. For complex, multi-component materials like High-Entropy Oxides (HEOs), differing sensitivities between EIS and GITT can lead to discrepancies in measured parameters due to multiple diffusion pathways. To further investigate the Li^+ diffusion kinetics in HEO and HEO@PPy, GITT was employed, and the data were processed using Equation (6) to determine the Li^+ diffusion coefficient:

$$D_{Li^+} = \frac{4}{\pi\tau}\left(\frac{m_B V_M}{M_B S}\right)^2 \left(\frac{\Delta E_S}{\Delta E_t}\right)^2 \quad (6)$$

where τ is the relaxation time of the constant current pulse, m_B is the mass of the active material loaded on the electrode, V_M is the molar volume of the active material,

M_B is the molar mass of the active material, S is the surface area of the electrode, ΔE_S is the total voltage change induced by the pulse, and ΔE_t is the voltage change during the constant-current charge/discharge step.

As shown in Fig. 6a, the plot of diffusion coefficient logarithm (logD) against voltage demonstrates that the HEO@PPy composite exhibits a higher Li^+ diffusion coefficient than bare HEO throughout the charge/discharge process. This indicates superior electrochemical kinetics, which can be attributed to the conductive network formed by the PPy coating that enhances the material's overall electrical conductivity. In the voltage–time profiles (Fig. 6b), HEO@PPy displays broader, more stable voltage plateaus with smaller fluctuations in logD, reflecting higher energy storage capacity and more stable cycling performance. These improvements stem from the flexible PPy coating, which buffers the volume expansion of HEO and acts as an interfacial barrier to suppress unstable solid electrolyte interphase (SEI) reconstruction. In summary, these results confirm that the PPy coating significantly enhances the Li^+ diffusion coefficient of HEO, findings that are consistent with EIS data.

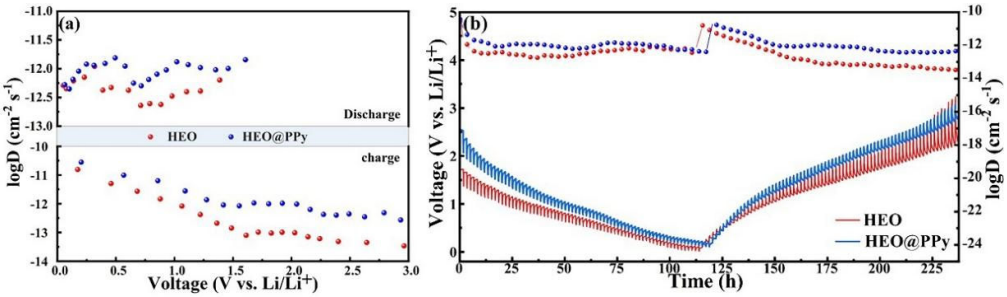

Fig. 6. HEO and HEO@PPy: Calculated logD versus voltage curves (a); GITT curves (b).

Table 1 summarizes the electrochemical performance of recently reported high-entropy oxides (HEOs) and their composites. The $(AlMnCoNiZn)_3O_4$@PPy material prepared in this study demonstrates excellent overall performance, with rate capability and long-cycle stability surpassing most reported materials. Notably, the performance of $(AlMnCoNiZn)_3O_4$ is significantly better than our previously reported $(CrMnCoNiZn)_3O_4$ [20], highlighting the critical role of Al substitution. Although Al is an electrochemically inert element that does not contribute to the total capacity, the high bond energy of Al-O prevents structural collapse during long-term cycling. This enhanced structural stability greatly improves the cycle life and rate performance of the HEO. Furthermore, the high conductivity and flexibility of PPy significantly improve the properties of both $(AlMnCoNiZn)_3O_4$ and $(CrMnCoNiZn)_3O_4$ upon compositing. In summary, the inert Al^{3+} enhances structural stability under long cycling conditions, while elemental reconfiguration optimizes the chemical environment for lithium storage, resulting in superior performance.

Table 1. Electrochemical performances of recently reported high entropy oxide anodes.

Composition	Rate capability / mAh g^{-1}	Cyclic performance (cycles) at low current / mAhg $^{-1}$	Cyclic performance (cycles) at heavy current / mAhg $^{-1}$	References
$(AlMnCoNiZn)_3O_4$	210 at 2 A g^{-1}	445(100)at 0.1 A g^{-1}	350(1000) at 1 A g^{-1}	This work
$(CrMnCoNiZn)_3O_4$	151 at 2 A g^{-1}	132(100)at 0.1 A g^{-1}	107(1000) at 1 A g^{-1}	[20]
$(AlMnCoNiZn)_3O_4$@PPy	403 at 2 A g^{-1}	695(100)at 0.1 A g^{-1}	675(1000) at 1 A g^{-1}	This work
$(CrMnCoNiZn)_3O_4$@PPy	360 at 2 A g^{-1}	809(100)at 0.1 A g^{-1}	449(1000) at 1 A g^{-1}	[20]
(MgCoNiCuZn)O	150 at 10 A g^{-1}	525(—)at 0.05 A g^{-1}	420(2500) at 1 A g^{-1}	[34]
$(CrMnFeCoCu)_3O_4$	168 at 2 A g^{-1}	676(100)at 0.1 A g^{-1}	150(1000) at 0.5 A g^{-1}	[35]
$(CrFeMnCoNiLi)_3O_4$	189 at 2 A g^{-1}	675(200)at 0.2 A g^{-1}	150(800) at 2 A g^{-1}	[36]
$(CrFeMnNiCo_x)_3O_4$ (x=2, 3, 4)	147 at 2A g^{-1}	520(100)at 0.2 A g^{-1}	100(3000) at 3 A g^{-1}	[37]
$(FeNiCrMnZn)_3O_4$@MOF	290 at 2 A g^{-1}	810(400)at 0.5 A g^{-1}	350(1130) at 2 A g^{-1}	[38]
(MgCoNiCuZn)O@GO	393 at 2 A g^{-1}	950(200)at 0.05 A g^{-1}	460(1000) at 1 A g^{-1}	[39]
$(FeCoNiCrMn)_3O_4$@LTO/C	280 at 2 A g^{-1}	685(100)at 0.1 A g^{-1}	1060(600) at 0.5 A g^{-1}	[40]

To further analyze the lithium-ion storage kinetics, we investigated the HEO@PPy composite anode to evaluate capacitive and diffusion-controlled effects. Fig. 7a presents the CV curves of the composite electrodes at varying scan rates from 0.1 mV/s to 1.0 mV/s. The integrated area under these curves represents the total charge storage capacity, comprising both diffusion-controlled and capacitive contributions. As the scan rate increases, the redox peaks exhibit more pronounced current densities. At a given potential and scan rate, the total current (i) can be deconvoluted into the diffusion-controlled current (i_{diff}), originating from slow Faradaic processes, and the capacitive current (i_{cap}), arising from surface-dependent charge storage mechanisms, as described by Equation (4):

$$i = i_{diff} + i_{cap} = av^b \quad (0.5 \leq b \leq 1) \tag{4}$$

where a and b are adjustable parameters. A b-value of 1 indicates purely capacitive behavior ($i = i_{cap}$), while b = 0.5 signifies fully diffusion-limited kinetics ($i = i_{diff}$). Intermediate b-values ($0.5 < b < 1$) suggest mixed charge storage mechanisms, with higher values denoting greater capacitive dominance.

Further quantitative analysis is presented in Fig. 7b, where the b-values derived from the linear fits of log(i) versus log(v) plots are 0.78 for the reduction peaks and 0.67 for the oxidation peak. These results confirm that the HEO@PPy composite anode exhibits hybrid lithium storage behavior with predominant capacitive characteristics. To delineate these contributions, the current response at fixed potentials was decoupled using Equation (5) to distinguish between (k_1v) and diffusion-controlled ($k_2v^{1/2}$) processes:

$$i = k_1 v + k_2 v^{1/2} \tag{5}$$

As shown in Figure 7c, capacitive effects account for approximately 70% of the total charge storage at a scan rate of 1.0 mV/s. Figure 7d further quantifies this trend, illustrating a progressive increase in capacitive contributions from 41% at 0.1 mV/s to 70% at 1.0 mV/s as scan rates increase. This enhanced capacitive behavior is attributed to both electric double-layer capacitance and Faradaic pseudocapacitance resulting

from Li^+ adsorption and desorption at the electrode-electrolyte interface.

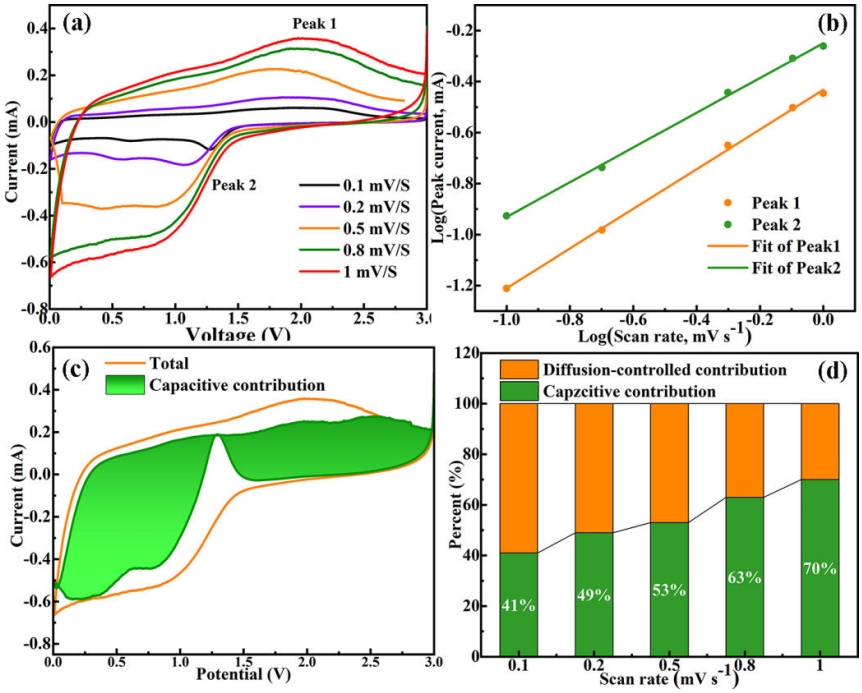

Fig. 7. Electrochemical kinetics analysis of HEO@PPy: CV curves at scan rates of 0.1–1.0 mV/s (a); Determination of b-values via log(i) vs. log(v) linear fitting (b); Capacitive charge storage contribution at 1.0 mV/s (c); Evolution of pseudocapacitive and diffusion-controlled contributions with increasing scan rate (d).

We performed XPS characterization on the HEO@PPy samples before and after cycling to analyze their elemental composition and valence states. Figures 8a and 8b present the survey spectra of HEO@PPy before and after cycling, respectively. The results indicate that the characteristic peaks of all elements remain present after cycling, suggesting the stability of the HEO@PPy structure. Furthermore, these peaks shift toward lower binding energies, which confirms that reduction reactions have occurred within the material.

The XPS spectra of Al 2p, Mn 2p, Co 2p, Ni 2p, Zn 2p, and O 1s (Figs. 8c-h) provide detailed information regarding spin-orbit peaks and the oxidation states of each element. As shown in Fig. 8c, the Al 2p binding energy is 74.85 eV before cycling and 74.66 eV after cycling, both corresponding to the Al^{3+} state. This indicates that Al does not participate in redox reactions, instead maintaining structural stability through high-bond-energy Al–O bonds [41]. In Fig. 8d, the Mn 2p spectrum exhibits typical spin-orbit splitting. Before cycling, Gaussian fitting reveals Mn^{4+} peaks (643.8 eV and 655.6 eV) and Mn^{3+} peaks (641.6 eV and 653.3 eV). After cycling, these peaks shift toward lower binding energies and a Mn^0 peak appears. This confirms a stepwise reduction from Mn^{4+}/Mn^{3+} to Mn^0 during lithiation, contributing to the electrochemical capacity through electron transfer and lithium-ion insertion [30]. The Co 2p spectrum (Fig. 8e) shows main peaks at 780.4 eV, 781.9 eV, 795.7 eV, and 797.1 eV, with satellite peaks at 784.8 eV and 803.1 eV. After cycling, the peaks shift toward lower binding energies,

Co^{2+} intensity increases, and a Co^0 peak appears. These results indicate that Co undergoes reduction during lithiation, serving as a core active component [40]. In Fig. 8f, the Ni 2p spectrum shows main peaks at 854.7 eV, 856.1 eV, 871.7 eV, and 873.3 eV, alongside satellite peaks at 860.4 eV and 879.8 eV, corresponding to Ni^{2+} and Ni^{3+}. After cycling, a Ni^0 peak appears and Ni^{3+} intensity decreases, indicating that Ni^{2+}/Ni^{3+} reduction contributes to the energy storage capacity of the HEOs [20]. Finally, the Zn 2p spectrum (Fig. 8g) displays sharp peaks at 1021.7 eV and 1044.8 eV, corresponding to Zn^{2+}. After cycling, these peaks shift toward lower binding energies without new impurity peaks, suggesting that Zn^{2+} undergoes a valence state reduction that contributes to the overall capacity [42].

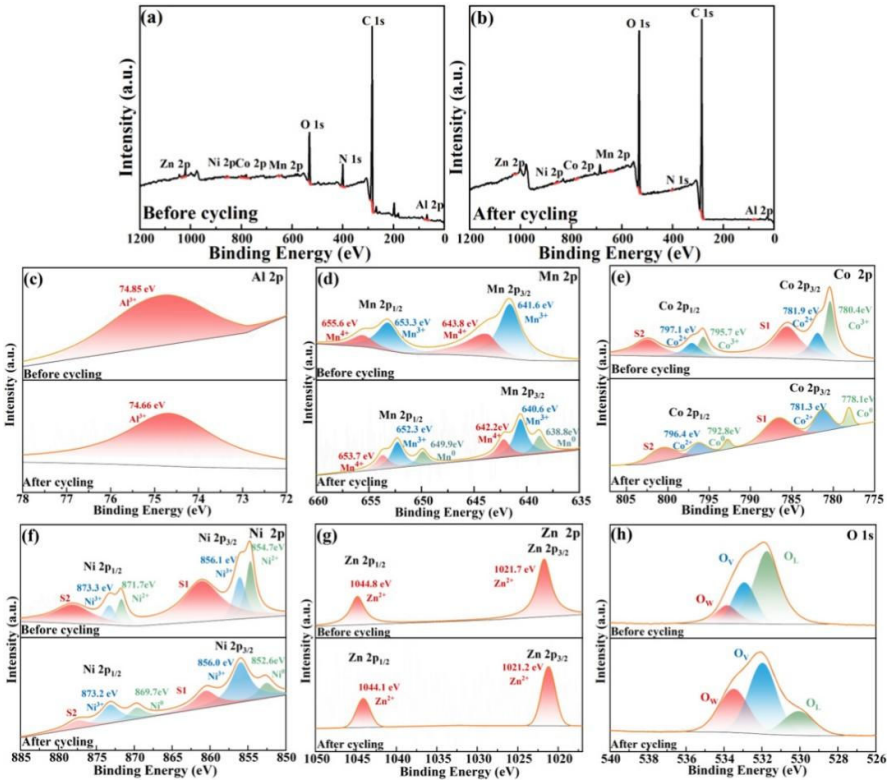

Fig. 8 XPS spectrogram of the HEO@PPy nanoparticles: (a) Before cycling full spectrum; (b) After cycling full spectrum; (c) Al 2p; (d) Mn 2p (c); (e) Co 2p; (f) Ni 2p; (g) Zn 2p; (h) O 1s.

The high-resolution O 1s spectrum in Fig. 8h can be decomposed into three components: adsorbed oxygen (O_W), defect oxygen (O_V), and lattice oxygen (O_L). O_W primarily corresponds to oxygen-containing species, such as physically or chemically adsorbed water molecules and hydroxyl groups on the material surface, reflecting the interfacial interaction between HEO@PPy and the electrolyte. O_V originates from undercoordinated oxygen species in the spinel lattice—including oxygen vacancies, interstitials, and antisite defects—which provide channels for lithium-ion diffusion. O_L forms stable metal-oxygen (M-O) covalent bonds (e.g., Al-O and Mn-O) and maintains the stability of the spinel AB_2O_4 lattice. Within this framework, A-site ions (typically +2/+4) and B-site ions (typically +3/+2) coordinate with O_L to form a stable

tetrahedral/octahedral structure. After cycling, the intensity of the lattice oxygen peak decreases significantly, indicating that O_L participates in redox reactions during lithiation. Simultaneously, the distribution and intensity of the surface adsorbed oxygen peak change significantly, corresponding to the formation and evolution of the SEI film. Composed primarily of oxygen-containing compounds, this SEI film reflects the electrochemical reversibility of HEO@PPy and confirms its excellent interfacial stability, which supports the material's enhanced long-cycle performance [43].

4. Conclusion

In summary, spinel-structured $(AlMnCoNiZn)_3O_4$ HEO nanoparticles were successfully synthesized via a solution combustion method, followed by the fabrication of $(AlMnCoNiZn)_3O_4$ @PPy composites through a stepwise approach. As LIB anode, the HEO@PPy composite electrode exhibits superior cycling stability and rate capability compared to pristine $(AlMnCoNiZn)_3O_4$ HEO nanoparticles. This enhanced electrochemical performance is attributed to several key factors: 1) The flexible PPy coating uniformly encapsulates the HEO particles, effectively buffering volume variations during Li+ insertion/extraction and mitigating capacity degradation. 2) The PPy layer suppresses excessive solid-electrolyte interphase (SEI) formation on the HEO surface, preventing detrimental side reactions and particle disintegration while improving ICE. 3) The conductive PPy matrix significantly improves the overall electrical conductivity of the composite, facilitating electron transport and enhancing rate performance. The $(AlMnCoNiZn)_3O_4$@PPy composite design provides a promising strategy that can be extended to other HEOs and conductive polymer systems.

CRediT authorship contribution statement

Yunhe Liang: Writing – original draft, Investigation, Formal analysis, Data curation. **Changqing Jin:** Writing – original draft, Supervision, Investigation, Funding acquisition, Formal analysis, Data curation, Conceptualization. **Dengyu Tian**: Writing – review & editing, Investigation, Formal analysis, Data curation. **Zaidong Peng:** Writing – review & editing, Investigation. **Zhong Yang:** Writing – review & editing, Investigation. **Qingping Ding:** Writing – review & editing, Writing – original draft, Investigation, Funding acquisition, Formal analysis.

Declaration of competing interest

The authors declare that they have no known competing financial interests or personal relationships that could have appeared to influence the work reported in this paper.

Data availability

Data used for the research described in the article can be found at: https://doi.org/10.5281/zenodo.18057734.

Acknowledgements

The work at Ames National Laboratory was supported by the U.S. Department of Energy, Division of Materials Sciences and Engineering. Ames National Laboratory is operated for the U.S. Department of Energy by Iowa State University under Contract No DE-AC02-07CH11358.

References

[1] M. M. Hasan, R. Haque, M. I. Jahirul, M. G. Rasul, I. M. R. Fattah, N. M. S. Hassan, M. Mofijur, **Advancing energy storage: The future trajectory of lithium-ion battery technologies,** Journal of Energy Storage, 120 (2025) 116511

[2] H. Sharma, S. Sharma, P. K. Mishra, **A critical review of recent progress on lithium ion batteries: Challenges, applications, and future prospects,** Microchemical Journal, 212 (2025) 113494

[3] H. Zhang, Y. Yang, D. Ren, L. Wang, X. He, **Graphite as anode materials: Fundamental mechanism, recent progress and advances,** Energy Storage Mater., 36 (2021) 147-170

[4] W. L. Zhai, X. T. Wu, J. Qian, X. X. Zuo, Y. H. Li, J. Gao, J. S. Yuan, Y. G. Xia, **Subcritical impurity removal and regeneration of spent graphite anodes achieving 99.5 % purity,** Carbon, 238 (2025) 120216

[5] W. Luo, J. Y. Jiao, J. Wang, Y. L. Duan, Z. H. Shen, **Understanding the microstructure effects of graphite electrode in lithium-ion batteries through multi-physics simulation,** Appl. Phys. Lett., 126 (2025) 123903

[6] Z. Zhang, Y. Wu, Z. Mo, X. Lei, X. Xie, X. Xue, H. Qin, H. Jiang, **Research progress of silicon-based anode materials for lithium-ion batteries,** RSC advances 15 (2025) 10731-10753

[7] H. Liu, S. Z. Wang, L. Liu, J. A. Zhao, W. J. Zhang, R. Bao, L. J. Wang, J. Q. Yang, Y. H. Li, Z. F. Jing, **Strategies, perspectives, and challenges of improving the initial coulombic efficiency and tap density of Sn-based anode materials for lithium-ion batteries,** Chem. Eng.

J., 495 (2024) 152444

[8] J. Wang, F. X. Song, Q. L. Chen, **S/Nb co-doped $Li_4Ti_5O_{12}$ as anode for high-rate lithium-ion batteries materials prepared by industrial H_2O_3Ti,** J. Energy Storage, 116 (2025) 116100

[9] J. J. Fang, K. C. Xie, Y. L. Song, K. Y. Zhang, F. Xu, X. Z. Shi, M. Ren, M. Z. Zhan, H. Lin, L. Y. Yang, S. N. Li, F. Pan, **Break the capacity limit of $Li_4Ti_5O_{12}$ anodes through oxygen vacancy engineering,** Chinese J. Struc. Chem., 44 (2025) 100504

[10] X. F. Liu, X. K. Li, Y. G. Li, H. J. Zhang, Q. L. Jia, S. W. Zhang, W. Lei, **High-entropy oxide: A future anode contender for lithium-ion battery**, Ecomat, 4 (2022) e12261

[11] C. M. Rost, E. Sachet, T. Borman, A. Moballegh, E. C. Dickey, D. Hou, J. L. Jones, S. Curtarolo, J. P. Maria, **Entropy-stabilized oxides,** Nat. Commun., 6 (2015) 8485

[12] A. Sarkar, L. Velasco, D. Wang, Q. Wang, G. Talasila, L. de Biasi, C. Kübel, T. Brezesinski, S.S. Bhattacharya, H. Hahn, B. Breitung, **High entropy oxides for reversible energy storage,** Nat. Commun., 9 (2018) 3400

[13] O. Marques, M. Walter, E. Timofeeva, C. Sagre, **Effect of initial structure on performance of high-entropy oxide anodes for li-ion batteries,** Batteries 9 (2023) 115

[14] X. Zou, Y. Zhang, Z. Huang, K. Yue, Z. Guo, **High-entropy oxides: an emerging anode material for lithium-ion batteries,** Chemical Communications 59 (2023) 13535-13550

[15] K. Wang, W. Hua, X. Huang, D. Stenzel, J. Wang, Z. Ding, Y. Cui, Q. Wang, H. Ehrenberg, B. Breitung, C. Kübel, X. Mu, **Synergy of cations in high entropy oxide lithium ion battery anode,** Nature Communications 14 (2023) 1487

[16] L. Wang, J. W. Han, D. B. Kong, Y. Tao, Q. H. Yang, Enhanced Roles of Carbon Architectures in High-Performance Lithium-Ion Batteries, Nano-Micro Lett., 11 (2019) 5

[17] L. D. Zhai, C. P. Hou, H. H. Sun, Y. Q. Qu, J. Hou, H. Lu, J. D. Wu, B. P. Wang, Y. Ma, X. X. Guo, **Polypyrrole in-situ coated SiO as anode material for lithium-ion batteries with excellent cyclic performance,** J. Energy Storage, 97 (2024) 112715

[18] K. Namsheer, S. Chandra, **Conducting polymers: a comprehensive review on recent advances in synthesis, properties and applications,** RSC advances 11 (2021) 5659-5697

[19] J. John, M. Manoj, A. Abhilash, S. Jayalekshmi, **On the improvement of the electrochemical behaviour of lithium-substituted polypyrrole for applications in Li-ion cells,** Ionics 27 (2021) 1733-1742

[20] C. Jin, Y. Wang, Y. Wei, R. Nan, Z. Jian, Z. Yang, Q. Ding, **$(CrMnCoNiZn)_3O_4$@PPy core-shell nanocomposite with excellent electrochemical performance as lithium-ion battery anode,** J. Power Sources, 613 (2024) 234926

[21] C. Jin, Y. Wang , H. Dong , Y. Wei, R. Nan, Z. Jian, Z. Yang and Q. Ding, **A Novel Spinel High-Entropy Oxide $(Cr_{0.2}Mn_{0.2}Co_{0.2}Ni_{0.2}Zn_{0.2})_3O_4$ as Anode Material for Lithium-Ion Batteries,** Inorganics, 12 (2024) 198

[22] C. Jin, Y. Wang, P. Lu, H. Dong, Y. Wei, R. Nan, Z. Jian, Z. Yang, Q. Ding, **Effect of crystallite size on lithium storage performance of high entropy oxide $(Cr_{0.2}Mn_{0.2}Co_{0.2}Ni_{0.2}Zn_{0.2})_3O_4$ nanoparticles,** Electrochem. Acta, 506 (2024) 145004

[23] G. Y. Wen, S. K. Zhong, X. P. Zhang, Z. H. Shi, B. J. Wang, Y. L. Sui, J. Zeng, Z. W. Zhang, L. Wu, **PPy modified 1T-MoS_2 hollow spheres with cohesive architecture as high-performance anode material for Li-ion batteries,** Ceram. Int., 48 (2022) 9781-9787

[24] H. Li, S. Yang, Y. Zhao, T. Tan, X. Wang, Z. Bakenov, **Synthesis of ZnO/Polypyrrole nanoring composite as high-performance anode materials for Lithium ion batteries,** J. Nanomater., 2019 (2019) 702849

[25] M. Setka, R. Calavia, L. Vojkuvka, E.Llobet, J. Drbohlavová, S. Vallejos, **Raman and XPS studies of ammonia sensitive polypyrrole nanorods and nanoparticles,** Sci. Rep., 9 (2019), 8465

[26] R. K. Mishra, F. B. Minussi, P. Kumari, R. R. Shahi, E.B. Araújo, **Synthesis and functional properties of $(Al_{0.2}Co_{0.2}Fe_{0.2}Ni_{0.2}Ti_{0.2})_3O_4$ high entropy spinel oxide,** J. Phys. Chem. Solids, 194 (2024) 112249

[27] R. K. Mishra, E. B. Araujo, R. R. Shahi, **Studies on synthesis, Raman, and electrical properties of novel spinel high entropy ceramics,** J. Electroceram., 10 (2024) 1007

[28] Chengjiao Che, Jianqiang Bi, Xihua Zhang, Yao Yang, Hongyi Wang, Jiacheng Rong **Synthesis and electrochemical performance of novel high-entropy spinel oxide $(FeCoMgCrLi)_3O_4$,** Electroanal. Chem., 974 (2024) 118719

[29] B. Xiao, G. Wu, T. Wang, Z. Wei, Y. Sui, B. Shen, J. Qi, F. Wei, J. Zheng, **High-entropy oxides as advanced anode materials for long-life lithium-ion Batteries,** Nano Energy, 95 (2022) 106962

[30] D. Wang, S. Jiang, C. Duan, J. Mao, Y. Dong, K. Dong, Z. Wang, S. Luo, Y. Liu, X. Qi, **Spinel-structured high entropy oxide $(FeCoNiCrMn)_3O_4$ as anode towards superior lithium storage performance,** J. Alloy. Compd., 844 (2020) 156158

[31] O. J. Marques, M. D. Walter, E. V. Timofeeva, C. U. Segre, **Effect of initial structure on performance of high-entropy oxide anodes for li-ion batteries,** Batteries., 9 (2023) 115

[32] T. Yi, L. Shi, X. Han, F. Wang, Y. Zhu, Y. Xie, **Approaching high-performance lithium storage materials by constructing hierarchical $CoNiO_2$@ CeO_2 nanosheets.** Energy & Environmental Materials., 4 (2021) 586-595

[33] Y. Tan, S. Li, Z. Huang, W. Kang, Y. Hua, X. Liu, G. Luo, X. Chen, J. Feng. **High-performance lithium storage anode: Polypyrrole-coated microrods BiSBr with conversion-alloying dual mechanism,** Chemical Engineering Journal (2025) 163178

[34] R. Ren, Y. Xiong, Z. Xu, J. Zhang, Y. Zhang, G. Zhu, K. Yin, S. Dong, **Fast synthesis of high-entropy oxides for lithium-ion storage,** Chemical Engineering Journal, 479 (2024) 147896

[35] L. Oroszova, D. Csik, G. Bortel, R. Dzunda, L. Temleitner, M. Hagarova, B. Breitung, K. Saksl, **Utilizing High-Capacity Spinel-Structured High-Entropy Oxide $(CrMnFeCoCu)_3O_4$ as a Graphite Alternative in Lithium-Ion Batteries,** Crystals, 14 (2024) 218

[36] C Liu, J. Bi, L. Xie, X. Gao, L. Meng, **Electrochemical properties of four novel high-entropy spinel oxides used as lithium-ion battery anodes synthesized by the glycine-nitrate SCS method,** Journal of Materials Science, 58 (2023) 8005-8021

[37] C. Liu, J. Bi, L. Xie, X. Gao, J. Rong, **High entropy spinel oxides $(CrFeMnNiCox)_3O_4$ (x= 2, 3, 4) nanoparticles as anode material towards electrochemical properties,** Journal of Energy Storage, 71 (2023) 108211

[38] Y. Luo, J. Li, X. Zhou, H. Dong, Y. Huang, P. Zhang, X. Huang, B. Yue, **Metal-organic framework-derived non-equimolar ratio inverse spinel-structured high-entropy oxides as anode materials for high-performance lithium-ion batteries,** Journal of Alloys and Compounds, 1008 (2024) 176515

[39] H. Guo, J. Shen, T. Wang, C. Cheng, H. Yao, X. Han, Q. Zheng, **Design and fabrication of high-entropy oxide anchored on graphene for boosting kinetic performance and energy storage,** Ceramics International,48 (2022) 3344-3350

[40] F. Zhai, S. Gao, W. Zhang, G. Cao, H. Zhang, Y. Xing, Y. Xiang, S. Zhang, **Surface-modified spinel high entropy oxide with hybrid coating-layer for enhanced cycle stability and lithium-ion storage performance,** RSC advances 14 (2024) 33124-33132

[41] X. Guo, P. Gu, J. Wu, K. Li, Y. Liang, G. Wang, Z. Zhang, C. Guo, **A novel Co-free high-entropy oxide $(FeNiCrMnMgAl)_3O_4$ as advanced anode material for lithium-ion batteries,** Journal of Electroanalytical Chemistry 978 (2025) 118910

[42] F. Ganjali, H. Arabi, S. R. Ghorbani, N. Azad, **Poperties of High-Entropy spinel oxides $(Mg_{0.2}X_{0.2}Zn_{0.2}Ni_{0.2}Fe_{0.2})_3O_4$ (X= Ti, Cr) as Lithium-Ion battery anodes,** Journal of Electroanalytical Chemistry 979 (2025) 118922

[43] F. Zhai, X. Zhu, W. Zhang, G. Cao, H. Zhang, Y. Xing, S. Zhang, **Insight of the evolution of structure and energy storage mechanism of $(FeCoNiCrMn)_3O_4$ spinel high entropy oxide**

in life-cycle span as lithium-ion battery anode, Journal of Power Sources 03 (2024) 234418